Transcranial photoacoustic tomography de-aberrated using boundary elements

Karteekeya Sastry, Yousuf Aborahama, Yilin Luo, Yang Zhang, Manxiu Cui, Rui Cao, Geng Ku, Lihong V. Wang, *Fellow, IEEE*

***Abstract*—Photoacoustic tomography holds tremendous potential for neuroimaging due to its functional magnetic resonance imaging (fMRI)-like functional contrast and greater specificity, richer contrast, portability, open platform, faster imaging, magnet-free and quieter operation, and lower cost. However, accounting for the skull-induced acoustic distortion remains a long-standing challenge due to the problem size. This is aggravated in functional imaging, where high accuracy is needed to detect minuscule functional changes. Here, we develop an acoustic solver based on the boundary-element method (BEM) to model the skull and de-aberrate the images. BEM uses boundary meshes and compression for superior computational efficiency compared to volumetric discretization-based methods. We demonstrate BEM's higher accuracy and favorable scalability relative to the widely used pseudo-spectral time-domain method (PSTD). In imaging through an ex-vivo adult human skull, BEM outperforms PSTD in several metrics. Our work establishes BEM as a valuable and naturally suited technique in photoacoustic tomography and lays the foundation for BEM-based de-aberration methods.**

***Index Terms*—Photoacoustic tomography, Transcranial imaging, Boundary element method**

I. INTRODUCTION

PHOTOACOUSTIC tomography [1] (PAT)—a hybrid imaging modality that combines optical excitation with ultrasound detection, thus enabling optical absorption imaging at sub-millimeter resolution and centimeter-level depth—has been developed for several clinically relevant applications, such as small-animal whole-body imaging [2], human extremity imaging [3], and human breast imaging [4]. Recently, PAT of the human brain was shown to have promise as a complementary neuroimaging modality [5], [6]. However, one key challenge remains, namely, the effect of the human skull on photoacoustic (PA) waves.

The adult human skull causes optical attenuation as well as acoustic attenuation and distortion, which degrade the PAT image quality [6]. While the optical and acoustic attenuation result in lower signal strength, the acoustic distortion severely aberrates the resulting transcranial images. This distortion is attributed to the starkly different acoustic properties of the skull relative to water or soft tissue, which results in the reflection and refraction as well as varying time or phase delays of acoustic waves. In addition to compression waves, the skull also supports shear waves, which causes mode-conversion at the interfaces. Finally, the skull induces dispersion and frequency-dependent attenuation, which broaden and attenuate wideband ultrasonic pulses. A PAT image reconstruction technique that can account for the skull is critical for developing PAT as a high-resolution neuroimaging technique.

One of the major challenges in developing image reconstruction algorithms for transcranial PAT (T-PAT) is the large problem size. For instance, at a frequency of 1 MHz, the computational domain is of the order of hundreds of wavelengths in each dimension. Despite this, a few approaches based on the finite-difference time-domain (FDTD) [7] and more recently [8] (in a preprint), the pseudo-spectral time-domain (PSTD) methods, respectively, accelerated on graphics processing units (GPUs), were employed for image reconstruction in three-dimensional (3D) T-PAT using an elastic model for the skull. However, coarse discretizations, necessitated by the large problem size and limited computational resources, result in low accuracy. Moreover, these methods scale poorly with the frequency. To improve the accuracy and overcome the staircasing effect in FDTD, the finite element method may be considered [9]. However, it is computationally infeasible in 3D due to the prohibitively large mesh size. To achieve high accuracy at a manageable and scalable computational cost, we propose to use the boundary element method (BEM) [10], a numerical technique for solving partial differential equations that can be formulated as boundary integrals.

Amongst popular methods, BEM is best suited to T-PAT for several reasons. First, BEM uses boundary/surface meshes instead of volumetric meshes/grids, which results in a significant reduction in the problem size, especially since a large part (~75% by volume) of the computational domain is water. The use of a surface mesh along with compression schemes [11] also makes BEM more scalable than the previously mentioned approaches at higher frequencies. Second, unlike many time-domain methods, such as FDTD and PSTD, the error in the computed field in BEM does not depend heavily on the propagation distance (~10– 15 cm in PAT). Additionally, BEM is naturally suited to open-boundary

This work was sponsored by the United States National Institutes of Health (NIH) grants U01 EB029823 (BRAIN Initiative), R35 CA220436 (Outstanding Investigator Award), and R01 CA282505. *(Karteekeya Sastry and Yousuf Aborahama contributed equally to this work.) (Corresponding author: Lihong V. Wang.)*

The authors are with the Caltech Optical Imaging Laboratory, Andrew and Peggy Cherng Department of Medical Engineering and the Department of Electrical Engineering, California Institute of Technology, Pasadena, CA 91125 USA (e-mail: sdharave@caltech.edu; y.aborahama@caltech.edu; yilinluo@caltech.edu; zoengy@caltech.edu; mccui@caltech.edu; ruicao@caltech.edu; gku@caltech.edu; lvw@caltech.edu)

problems and does not require absorbing layers. Third, surface meshes in BEM accurately capture the geometry of the scatterers without suffering from staircasing. Furthermore, we can place sources and detectors anywhere, without needing to re-mesh or interpolate. Last, since we implement BEM in the frequency domain, we can naturally incorporate frequency-dependent attenuation and dispersion, if necessary. For these reasons, BEM has been used in medical ultrasound to simulate transcranial [12] and transcostal [13] acoustic propagation.

II. METHODS

A schematic of T-PAT is depicted in Fig. 1a, which illustrates the source of illumination, the object being imaged (i.e., an adult human head including the scalp, skull, and brain), the ultrasound coupling medium (water), and a hemispherical ultrasonic detection surface. Since the most prominent optical absorbers in the brain at the wavelengths of interest (700–1100 nm) are oxy- and deoxy-hemoglobin [14] (see the left panel of Fig. 1b), blood vessels are the predominant features in PAT images, as shown in the top-right of Fig. 1a. The skull causes reflection, refraction, and mode conversion of the incident PA waves at the brain-skull and skull-scalp interfaces, as depicted in the inset to the right of Fig. 1a. The intensity transmittances at the two interfaces [15] for representative skull and brain/scalp properties [6] are summarized in the center and right panels of Fig. 1b, respectively, which elucidate the various effects the skull has on acoustic waves. Next, we present the mathematical derivation of our BEM-based acoustic solver.

A. Photoacoustic imaging: initial pressure generation

Photoacoustic imaging is based on the generation of acoustic waves due to the absorption of light by tissue [1], i.e., the photoacoustic effect. The fractional volume expansion of tissue, dV/V, due to light absorption, can be written as [16],

$$\frac{dV}{V} = -\kappa p + \beta T, \tag{1}$$

where κ (Pa^{-1}) and β (K^{-1}) denote the isothermal compressibility and thermal coefficient of volume expansion, respectively, and p and T denote the rise in pressure and temperature, respectively. When conditions of thermal and stress confinement are satisfied (i.e., when the laser pulse duration is shorter than the thermal and stress relaxation times), the fractional volume expansion is negligible, and the local temperature rise due to the laser excitation gets converted to a pressure rise, p_0, which can be related to the optical absorption coefficient (μ_a; m^{-1}) and the optical fluence (F; $\mathrm{J/m}^2$) as

$$p_0 \propto \mu_a F. \tag{2}$$

The photoacoustic wave propagation due to the initial pressure distribution, $p_0(\boldsymbol{r})$, in a lossless, homogeneous, fluid medium at a frequency f is governed by the inhomogeneous Helmholtz equation:

$$(\Delta + k^2)p(\boldsymbol{r}) = -\frac{2\pi j f}{v^2} p_0(\boldsymbol{r}), \tag{3}$$

where Δ is the Laplacian operator, k is the wave number of acoustic waves in the medium at f, v is the speed of sound in the medium, and $p(\boldsymbol{r})$ is the pressure at the location $\boldsymbol{r}$. Here, we adopt the convention that the Fourier transform of the function, $h(t)$, is given by $H(f) = \int_{-\infty}^{\infty} h(t)e^{-j2\pi ft}dt$.

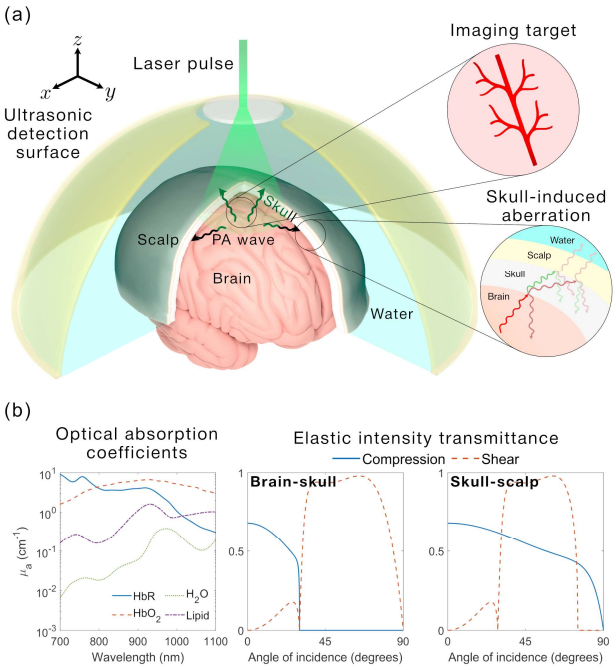

Fig. 1| Schematic of T-PAT. (a) Schematic of T-PAT, which shows the laser pulse, the imaging target (a human head including the scalp, skull, and brain), the ultrasound coupling medium (water), and a hemispherical ultrasonic detection surface. Top-right: The imaging targets are primarily comprised of blood vessels since hemoglobin is the most dominant optical absorber in the wavelengths of interest. Right: The generated PA waves undergo reflection, refraction, and mode-conversion at the brain-skull and skull-scalp interfaces. Compression (longitudinal) waves and shear waves are shown using red and green arrows, respectively. (b) Left: Optical absorption coefficients of the most prominent optical absorbers in tissue. Center: Intensity transmittances of the transmitted compression and shear waves at the brain-skull interface, respectively. Right: Intensity transmittances of the transmitted compression waves for compression and shear wave incidence at the skull-scalp interface, respectively.

B. Mathematical formulation of BEM

Consider a regular closed surface Γ that partitions $\mathbb{R}^3$ into an exterior region V_1 and an interior region V_2. Each V_i contains a homogeneous medium with a speed of sound and density of v_i and ρ_i, respectively for $i = 1, 2$. The exterior region, V_1, contains an acoustic source, $s(\boldsymbol{r})$, and V_2 is source-free. In the case of T-PAT, V_2 comprises the skull and V_1 comprises everything outside the skull (i.e., soft tissue and water). Let $p_1 : V_1 \to \mathbb{C}$ and $p_2 : V_2 \to \mathbb{C}$ be twice continuously differentiable functions that represent the pressure in V_1 and V_2, respectively. Then, p_1 and p_2 satisfy the Helmholtz equation [17].

$$(\Delta + k_i^2)p_i(\boldsymbol{r}) = \delta_{i1}s(\boldsymbol{r}), \qquad \boldsymbol{r} \in V_i,\ i = 1, 2, \tag{4}$$

where k_1 and k_2 are the wave numbers of acoustic waves in V_1 and V_2, respectively, at f, and δ_{ij} denotes the Kronecker delta. We consider the following fundamental solution of the Helmholtz equation that satisfies the Sommerfeld radiation condition [18].

$$g_i(\boldsymbol{r}, \boldsymbol{r}') = \frac{e^{jk_i|\boldsymbol{r}-\boldsymbol{r}'|}}{4\pi|\boldsymbol{r}-\boldsymbol{r}'|}, \qquad \boldsymbol{r} \neq \boldsymbol{r}', \qquad i = 1, 2, \tag{5}$$

where $|\boldsymbol{r}|$ denotes the magnitude of the vector $\boldsymbol{r}$. Using Green's identities, the solution can be expressed as [18],

$$\begin{aligned}(-1)^{i+1}p_i(\boldsymbol{r}) = &\oint_\Gamma g_i(\boldsymbol{r},\boldsymbol{r}')\frac{\partial \hat{p}_i(\boldsymbol{r}')}{\partial \boldsymbol{n}'}d\gamma' \\ &- \oint_\Gamma \hat{p}_i(\boldsymbol{r}')\frac{\partial g_i(\boldsymbol{r},\boldsymbol{r}')}{\partial \boldsymbol{n}'}d\gamma' \\ &+ \delta_{i1}p^{\text{inc}}(\boldsymbol{r}), \quad \boldsymbol{r}\in V_i, \quad i=1,2,\end{aligned} \tag{6}$$

where $d\gamma'$ is a differential area element on the surface Γ in the primed coordinates, $\partial/\partial\boldsymbol{n}'$ is the derivative (in the primed coordinates) along the outward-pointing normal of Γ, $\hat{p}_i$ and $\partial\hat{p}_i/\partial\boldsymbol{n}'$ are the Dirichlet and Neumann traces of p_i, respectively, on the surface Γ for $i=1,2$, and $p^{\text{inc}}(\boldsymbol{r}) = \int_{V_1} g_1(\boldsymbol{r},\boldsymbol{r}')s(\boldsymbol{r}')d\boldsymbol{r}'$ is the incident field in V_1. This equation is known as the Green's representation theorem for the Helmholtz equation, and it relates the pressure and its normal derivative on the surface Γ to the pressure everywhere in V_i.

Similarly, on the surface, Γ, we have

$$\begin{aligned}(-1)^{i+1}C(\boldsymbol{r})\hat{p}_i(\boldsymbol{r}) = &\oint_\Gamma g_i(\boldsymbol{r},\boldsymbol{r}')\frac{\partial \hat{p}_i(\boldsymbol{r}')}{\partial \boldsymbol{n}'}d\gamma' \\ &- \oint_\Gamma \hat{p}_i(\boldsymbol{r}')\frac{\partial g_i(\boldsymbol{r},\boldsymbol{r}')}{\partial \boldsymbol{n}'}d\gamma' \\ &+ \delta_{i1}p^{\text{inc}}(\boldsymbol{r}), \quad \boldsymbol{r}\in\Gamma,\ i=1,2,\end{aligned} \tag{7}$$

and

$$\begin{aligned}(-1)^{i+1}C(\boldsymbol{r})&\frac{\partial \hat{p}_i(\boldsymbol{r})}{\partial \boldsymbol{n}} \\ &= \oint_\Gamma \frac{\partial g_i(\boldsymbol{r},\boldsymbol{r}')}{\partial \boldsymbol{n}}\frac{\partial \hat{p}_i(\boldsymbol{r}')}{\partial \boldsymbol{n}'}d\gamma' \\ &- \oint_\Gamma \hat{p}_i(\boldsymbol{r}')\frac{\partial^2 g_i(\boldsymbol{r},\boldsymbol{r}')}{\partial \boldsymbol{n}\,\partial \boldsymbol{n}'}d\gamma' \\ &+ \delta_{i1}\frac{\partial p^{\text{inc}}(\boldsymbol{r})}{\partial \boldsymbol{n}}, \quad \boldsymbol{r}\in\Gamma,\ i=1,2.\end{aligned} \tag{8}$$

$C(\boldsymbol{r})$ is a real function that depends on the geometry of Γ around $\boldsymbol{r}$. For a smooth surface, such as the ones we consider here, it evaluates to ½ [18].

Finally, by imposing continuity of pressure and particle velocity on both sides of the interface [15], we obtain the following relations between $\hat{p}_1(\boldsymbol{r})$, $\hat{p}_2(\boldsymbol{r})$, $\partial\hat{p}_1(\boldsymbol{r})/\partial\boldsymbol{n}$, and $\partial\hat{p}_2(\boldsymbol{r})/\partial\boldsymbol{n}$ on Γ.

$$\hat{p}_1(\boldsymbol{r}) = \hat{p}_2(\boldsymbol{r});\ \frac{1}{\rho_1}\frac{\partial \hat{p}_1(\boldsymbol{r})}{\partial \boldsymbol{n}} = \frac{1}{\rho_2}\frac{\partial \hat{p}_2(\boldsymbol{r})}{\partial \boldsymbol{n}},\ \ \boldsymbol{r}\in\Gamma. \tag{9}$$

Eqns. (7) – (9), constructed on Γ, can be solved for the Dirichlet and Neumann traces of the interior and exterior pressures on Γ, which can in turn be plugged into Eq. (6) to compute the pressure everywhere. This captures the fundamental idea of the boundary element method (BEM).

To aid the solution of Eqns. (7) – (9), we discretize $\hat{p}_1(\boldsymbol{r})$ and $\partial\hat{p}_1(\boldsymbol{r})/\partial\boldsymbol{n}$, on the surface Γ, in a finite-dimensional space using a set of basis functions, $\{\phi_i(\boldsymbol{r})\}_{n=1}^N$, defined on Γ, as follows:

$$\begin{aligned}\hat{p}_1(\boldsymbol{r}) &\approx \sum_n a_n\phi_n(\boldsymbol{r}); \\ \frac{\partial \hat{p}_1(\boldsymbol{r})}{\partial \boldsymbol{n}} &\approx \sum_n b_n\phi_n(\boldsymbol{r}),\ \boldsymbol{r}\in\Gamma,\end{aligned} \tag{10}$$

where $a_n, b_n \in \mathbb{C}, n = 1, 2, \ldots, N$ are the coefficients of the basis functions and $\oint_\Gamma \phi_n(\boldsymbol{r})d\gamma = 1$.

Substituting Eq. (9) into Eqs. (7) and (8) for $i=2$, and taking an inner product on both sides of Eqs. (7) and (8) for $i=1,2$, (after substituting the basis expansion in Eq. (10)) with a set of testing functions, $\{\psi_n(\boldsymbol{r})\}_{n=1}^N$ (which are chosen here to be the same as the basis functions), we get the following linear equations.

$$\begin{aligned}\frac{\boldsymbol{a}}{2} &= V_1\boldsymbol{b} - K_1\boldsymbol{a} + \boldsymbol{a}^{\text{inc}}; \\ \frac{\boldsymbol{b}}{2} &= K_1'\boldsymbol{b} + W_1\boldsymbol{a} + \boldsymbol{b}^{\text{inc}};\end{aligned} \tag{11}$$

$$\begin{aligned}\frac{\boldsymbol{a}}{2} &= -V_2\boldsymbol{b} + K_2\boldsymbol{a}\ ; \\ \frac{\boldsymbol{b}}{2} &= -K_2'\boldsymbol{b} - W_2\boldsymbol{a}.\end{aligned} \tag{12}$$

Here, $\boldsymbol{a} = [a_1, a_2, \ldots, a_N]^T$, $\boldsymbol{b} = [b_1, b_2, \ldots, b_N]^T$, and V_i, K_i, K_i', and W_i $(i=1,2)$ are the scaled single-layer, double-layer, adjoint double-layer, and hypersingular boundary potential operators, and are defined as follows:

$$\begin{aligned}[V_i]_{mn} &= \frac{\rho_i}{\rho_1}\oint_\Gamma\oint_\Gamma g_i(\boldsymbol{r},\boldsymbol{r}')\phi_n(\boldsymbol{r}')\psi_m(\boldsymbol{r})d\gamma'd\gamma; \\ [K_i]_{mn} &= \oint_\Gamma\oint_\Gamma \frac{\partial g_i(\boldsymbol{r},\boldsymbol{r}')}{\partial \boldsymbol{r}'}\phi_n(\boldsymbol{r}')\psi_m(\boldsymbol{r})d\gamma'd\gamma; \\ [K_i']_{mn} &= \oint_\Gamma\oint_\Gamma \frac{\partial g_i(\boldsymbol{r},\boldsymbol{r}')}{\partial \boldsymbol{r}}\phi_n(\boldsymbol{r}')\psi_m(\boldsymbol{r})d\gamma'd\gamma; \\ [W_i]_{mn} &= -\frac{\rho_1}{\rho_i}\oint_\Gamma\oint_\Gamma \frac{\partial^2 g_i(\boldsymbol{r},\boldsymbol{r}')}{\partial \boldsymbol{r}\partial \boldsymbol{r}'}\phi_n(\boldsymbol{r}')\psi_m(\boldsymbol{r})d\gamma'd\gamma.\end{aligned} \tag{13}$$

Here, $[M]_{mn}$ denotes the element in the m^{th} row and the n^{th} column of the matrix M. The vectors $\boldsymbol{a}^{\text{inc}}$ and $\boldsymbol{b}^{\text{inc}}$ are defined as

$$\begin{aligned}\boldsymbol{a}_n^{\text{inc}} &= \oint_\Gamma p^{\text{inc}}(\boldsymbol{r})\psi_n(\boldsymbol{r})d\gamma; \\ \boldsymbol{b}_n^{\text{inc}} &= \oint_\Gamma \frac{\partial p^{\text{inc}}(\boldsymbol{r})}{\partial \boldsymbol{n}}\psi_n(\boldsymbol{r})d\gamma,\end{aligned} \tag{14}$$

where $[\boldsymbol{m}]_n$ denotes the n^{th} element of the vector $\boldsymbol{m}$. This approach, termed the Galerkin method, has the advantage that it results in a symmetric system of equations and can be readily coupled with the finite element method [10], [19].

Eqs. (11) and (12) can be concisely written as

$$\begin{aligned}\begin{bmatrix}\boldsymbol{a}\\ \boldsymbol{b}\end{bmatrix} &= \left(\frac{1}{2}I + A_1\right)\begin{bmatrix}\boldsymbol{a}\\ \boldsymbol{b}\end{bmatrix} + \begin{bmatrix}\boldsymbol{a}^{\text{inc}}\\ \boldsymbol{b}^{\text{inc}}\end{bmatrix}; \\ \begin{bmatrix}\boldsymbol{a}\\ \boldsymbol{b}\end{bmatrix} &= \left(\frac{1}{2}I - A_2\right)\begin{bmatrix}\boldsymbol{a}\\ \boldsymbol{b}\end{bmatrix},\end{aligned} \tag{15}$$

where $A_i = \begin{bmatrix}-K_i & V_i\\ W_i & K_i'\end{bmatrix}$, $i=1,2$ are scaled Calderón matrices. Note that the matrices $\left(\frac{1}{2}I + A_1\right)$ and $\left(\frac{1}{2}I - A_2\right)$ are idempotent [20]. Equating the right-hand sides of the two equations above yields

$$(A_1 + A_2)\begin{bmatrix}\boldsymbol{a}\\ \boldsymbol{b}\end{bmatrix} = \begin{bmatrix}\boldsymbol{a}^{\text{inc}}\\ \boldsymbol{b}^{\text{inc}}\end{bmatrix}. \tag{16}$$

This formulation has the advantage that $A_1 + A_2$ is self-regularizing, since $A_1^2 = A_2^2 = I/4$.

C. Implementation of BEM

We implemented all the operators described in Eq. (13) in MATLAB R2023b using the Gypsilab package [21]. We employed a continuous and piecewise affine set of basis functions defined on a triangular mesh for the fields on the surface. We used the same set of functions as our testing functions. We computed all the integrals using a three-point Gauss quadrature rule, chosen to optimize accuracy and speed. The integrals shown in Eq. (13) have a singularity when $\boldsymbol{r} \to \boldsymbol{r}'$. We deal with this by computing the singular part of the integral over $\boldsymbol{r}$ analytically, and then over $\boldsymbol{r}'$ numerically using the same quadrature rule [21]. Additional care is needed, however, in evaluating the hypersingular operators (W_i, $i = 1, 2$), which are first converted into weakly singular integrals using integration by parts [17]. The matrices constructed in BEM are dense, which limits their applicability to large-scale problems due to memory constraints. To overcome this, matrix compression methods such as the fast multipole method (FMM) or hierarchical matrix compression are used [11]. Here, we use the fast and free memory method (FFM) [22] for assembling the operators, which has a linear storage complexity and quasilinear computation complexity for matrix-vector products. We apply Calderón preconditioning [23] and use the generalized minimum residual (GMRES) method [24] to solve the linear system of equations.

III. RESULTS

A. Benchmarking the BEM implementation

To benchmark the accuracy of our BEM solver, we simulated the scattering of waves from a point source by a sphere with different acoustic properties. The background medium is assumed to be water and has a density and speed of sound of $1000\ \text{kg/m}^3$ and $1500\ \text{m/s}$, respectively. The sphere is centered at the origin. It has a radius of 5 cm and a density and speed of sound of $1800\ \text{kg/m}^3$ and $3000\ \text{m/s}$, respectively. The size and properties of the sphere are chosen to mimic those of the human skull [6]. The simulation setup, overlaid with the field amplitude at a single frequency, is shown in Fig. 2a.

A time-varying point source is placed at $(-12, 0, 0)$ cm which radiates a Gaussian-modulated sinusoidal pulse (shown in Fig. 2b) of the form $\exp(-\alpha f_0^2(t - t_0)^2)\sin(2\pi f_0 t)$, where $\alpha = 3.2$, $t_0 = 25\ \mu\text{s}$, and $f_0 = 0.05$ MHz is the center frequency of the pulse. The pulse has a 6 dB bandwidth of approximately 0.033 MHz. We pick this frequency range because it allows us to simulate the problem at very fine discretizations, which are necessary to comprehensively study the trade-offs between run-time and accuracy. The field is recorded at 32 positions in a circle of radius 8 cm centered at the origin in the $z = 0$ plane. The positions are chosen to be exactly on the grid in PSTD (at all discretizations) to avoid interpolation errors.

To compute the analytical solution, we first expand the incident field from a point source outside a sphere of radius, a, at each frequency as an infinite summation of Legendre polynomials [25]. Then, we match the boundary conditions (see Eq. (9)) on both sides of the sphere and leverage the orthogonality of the Legendre polynomials to arrive at the following solution.

$$p_{\text{out}}(r,\theta) = \sum_{n=1}^{\infty} \frac{(2n+1)jk_o}{4\pi} \frac{n_k j_n(k_o a) j_n'(k_i a) - n_d j_n'(k_o a) j_n(k_i a)}{n_d j_n(k_i a) h_n^{(1)\prime}(k_o a) - n_k j_n'(k_i a) h_n^{(1)}(k_o a)} h_n^{(1)}(k_o r_0) h_n^{(1)}(k_o r) P_n(\cos(\theta))\,; \tag{17}$$

$$p_{\text{in}}(r,\theta) = \sum_{n=1}^{\infty} \frac{(2n+1)jk_o}{4\pi} \frac{n_d h_n^{(1)\prime}(k_o a) j_n(k_o a) - n_d h_n^{(1)}(k_o a) j_n'(k_o a)}{n_d j_n(k_i a) h_n^{(1)\prime}(k_o a) - n_k j_n'(k_i a) h_n^{(1)}(k_o a)} h_n^{(1)}(k_o r_0) j_n(k_i r) P_n(\cos(\theta)). \tag{18}$$

Here $p_{\text{out}}(r,\theta)$ and $p_{\text{in}}(r,\theta)$ are the scattered field outside the sphere and the field inside the sphere, respectively; $n_d = \rho_i/\rho_o$ and $n_k = k_i/k_o$, where ρ_i and ρ_o are the densities of the sphere and the background medium, respectively, and k_i and k_o are the wave numbers in the sphere and the background medium; r_0 is the distance of the source from the origin, r is the magnitude of the position vector of the evaluation point, and θ is the angle between the position vector of the evaluation point and the source; j_n, $h_n^{(1)}$, and P_n denote the n^{th} order spherical Bessel function of the first kind, spherical Hankel function of the first kind, and Legendre polynomial, respectively, and $(\cdot)'$ denotes the derivative of a function. After computing the solution at each frequency, we take an inverse Fourier transform, after appropriately weighting with the frequency components of the source function, to arrive at the time-domain waveform received by the detector.

Since our BEM is formulated in the frequency domain, to compute the received pressure using BEM, we first transform the transmitted waveform to the frequency domain. We simulate a maximum frequency of 0.14 MHz and a signal duration of 1 ms, which results in a total of 140 frequency points. At each frequency, we use BEM to solve for the fields on the sphere, and therefore the field everywhere. We mesh the surface of the sphere by subdividing a triangular mesh of an icosahedron, which gives us a highly uniform mesh. The discretization level is changed by changing the degree of subdivision of the icosahedron mesh. For comparison, we simulated the same benchmark problem using PSTD. We used k-Wave [26], an open-source PSTD-based acoustic simulation toolbox, for the comparison. We simulated the benchmark problem within a $30\ \text{cm} \times 30\ \text{cm} \times 15\ \text{cm}$ computational domain at various levels of discretization. We terminated the computational domain with a perfectly matched layer (PML) to ensure that waves are not spuriously reflected into the domain.

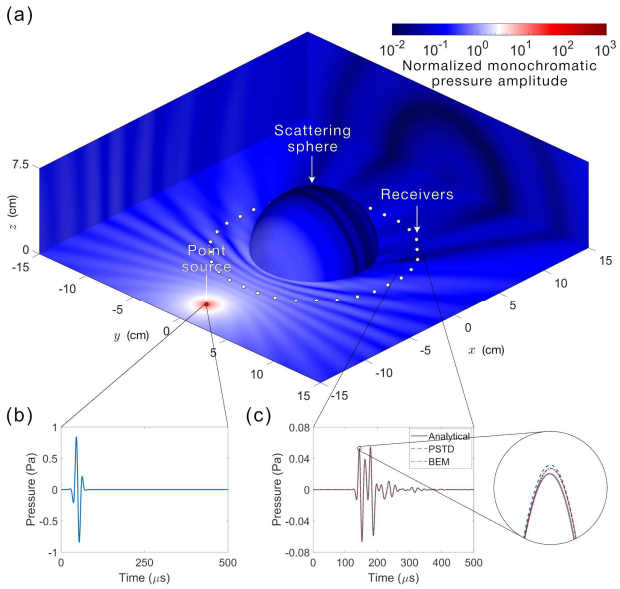

Fig. 2| Schematic of the BEM benchmarking problem. (a) Setup of the BEM benchmarking problem overlaid with the amplitude of the field at a single frequency. (b) Plot of the Gaussian-modulated sinusoidal pulse transmitted from the point source shown in (a). (c) Plot of the waveform received by a representative detector, computed using BEM and PSTD, overlaid on the analytical solution.

Finally, to verify the implementations, we plot the computed time-domain waveform at one of the detectors using BEM and PSTD, respectively, along with the analytical solution in Fig. 2c, which shows good agreement between the three plots.

We vary the discretization levels (number of points per wavelength in the mesh/grid) in BEM and PSTD and plot the run time of each method with its accuracy, calculated as the average of the relative root-mean-square error (RMSE) with respect to the analytical solution at all 32 positions, in Fig. 3a. This plot shows that while PSTD is faster than BEM at lower accuracies, BEM performs better at higher accuracies due to its favorable scalability. Further, although PSTD implemented on a GPU will be faster than BEM, it is not feasible beyond a certain problem size due to GPU memory limits. In Fig. 3b, we see that at a frequency of 0.1 MHz and for a given discretization level, BEM is always more accurate than PSTD. For the two cases encircled in Fig. 3a, which correspond to BEM and PSTD solutions with comparable accuracy and run time, we show the absolute errors in the scattered field for these two cases in the $z = 0$ plane at a single frequency (of 0.1 MHz), normalized to the maximum error in the two plots, in Figs. 3c and 3d, respectively. While BEM has a relatively uniform error in all directions, PSTD has a much higher error on the side of the sphere towards the source. This is because BEM analytically computes the incident field. Therefore, the error only exists in the scattered field, whereas PSTD propagates the source on the grid, thus incurring errors in both the incident and scattered fields. Finally, we also run the benchmark problem with a discretization of $\lambda/5$ at higher frequencies of 0.2 MHz, 0.3 MHz, 0.4 MHz, and 0.5 MHz and obtain similar relative RMSEs of 1.5%, 2.6%, 3.1%, and 2.6%, respectively. This shows that the method is accurate even at these higher frequencies.

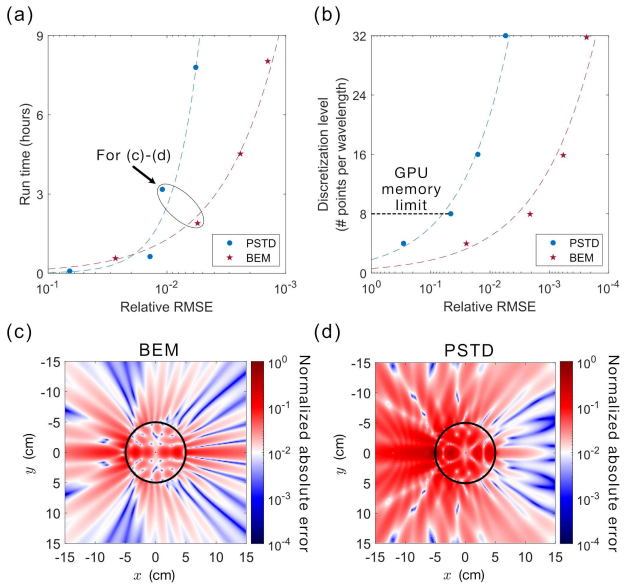

Fig. 3| Benchmarking the BEM. (a) Plot of run time versus accuracy (relative RMSE) for PSTD and BEM. It shows that BEM outperforms PSTD at higher accuracies due to its favorable scalability. (b) Plot of discretization level versus accuracy (average relative RMSE) for BEM and PSTD at a single frequency. For a given accuracy level, BEM requires a lower discretization level than PSTD. Discretization level is defined as the number of points per wavelength (in water) in the mesh/grid. (c)-(d) Plots of the absolute error in the scattered field in the z = 0 plane obtained using (c) BEM and (d) PSTD, normalized to the maximum error in the two plots, respectively, for the two cases encircled in (a) at a frequency of 0.1 MHz. While the error in the BEM solution is relatively uniform in all directions, the PSTD solution has a higher error on the side of the sphere towards the point source.

B. Experimental setup

We experimentally demonstrated the application of BEM in T-PAT by correcting the aberrations in phantom images acquired through an ex-vivo human skull. We used a 3D PAT system similar to the one described here [4], where the measurements are obtained using four rotating arc-shaped ultrasonic transducer arrays. We used deionized water as the background medium and placed the skull in the imaging field of view. To prevent air from being trapped inside the ex-vivo skull, we immersed the skull in water overnight and pumped air out of it using a vacuum pump. We attached fiducial markers, comprising light-absorbing points, to the skull at locations that were identifiable on the X-ray computed tomography (CT) volume of the skull. We used these markers to co-register the CT volume with the PAT volume. Phantoms, made from black wires, were attached to custom-made 3D-printed mounts for repeatability, and positioned close to the inner surface of the skull one at a time. The phantoms were illuminated from inside the skull using diffuse 1064 nm laser light to improve the signal-to-noise ratio (SNR) of the measurements and to reduce the spurious background from the skull, which might confound our study on the effectiveness of de-aberration through the skull. Note that this illumination scheme differs from the illustration shown in Fig. 1, which aims to depict a schematic and describe the physics of in-vivo T-PAT. Previous studies have already demonstrated that illuminating from outside the skull results in sufficient SNR for T-PAT [6].

C. Transcranial PAT image reconstruction procedure

The photoacoustic signals from the phantoms are acquired at a sampling frequency of 10 MHz and over a duration of 200 μs. Based on the geometry of the detection surface and the placement of the phantoms, we truncated the signal to discard those parts that are not of interest. Then, we transformed the signal to the frequency domain and picked a minimum and maximum frequency of 0.2 MHz and 0.5 MHz, respectively. These values were chosen due to the relatively low SNR of the detector elements at lower frequencies and the increased attenuation and scattering of the skull at higher frequencies [6]. Since we are using an acoustic model of the skull, additional care is taken to only use those elements where the shear waves from the skull have less importance. To do this, we consider those detectors that subtend an angle less than 45° at the center of the reconstruction region with respect to the skull normal.

We use iso2mesh [27], an open-source MATLAB package, to mesh the CT volume of the skull. To reduce the problem size, we only simulate the part of the skull that lies between the reconstructed region and the detector array. We ensure that the mean element size in the mesh at each frequency is close to $\lambda/5$ and that the maximum element size does not exceed $\lambda/2$, where λ is the wavelength in water. The resulting mesh has around 10^4 elements at the lowest frequency and 10^5 elements at the highest one. To reconstruct an image, we treat the detectors as point sources that radiate the time-reversed (phase-conjugated in frequency domain) received waveform and record the pressure at the last time instant (by scaling the computed fields with the frequency response and summing up the fields at all the frequencies). We used a speed of sound and density in water of 1482 m/s and 1000 kg/m^3, respectively, and in the skull of 2800 m/s and 1800 kg/m^3, respectively. The parameters for the skull were obtained by tuning the parameters within their respective physiological ranges to optimize image quality.

For comparison, we also reconstructed transcranial images using PSTD [26]. The signals were low-pass filtered to 0.5 MHz using a 6$^{\text{th}}$ order Butterworth filter, time-reversed, and specified as a Dirichlet boundary condition. We simulated a 28 cm × 28 cm × 15 cm grid that was discretized at 0.5 mm, which is around one-sixth of a wavelength at 0.5 MHz. The pressure at the final instant was recorded as the reconstructed image. Finally, we display the maximum amplitude projections (MAPs) of the reconstructed volumes.

To verify and preliminarily demonstrate the BEM-based reconstruction scheme, we conducted numerical phantom reconstruction experiments and report them in Appendix A. Further, the X-ray CT volume used for extracting the ex-vivo skull surface in this work was obtained at a resolution of 0.35 mm. To test whether this resolution provides a sufficiently accurate surface mesh for BEM reconstruction, we study the impact of edge-modeling accuracy on BEM in Appendix B.

D. Experimental results

We acquired images of light-absorbing phantoms through an ex-vivo adult human skull. We also image the same phantoms without the skull and consider the resulting image, reconstructed using the universal back-projection algorithm (UBP) [28], to be the ground truth. Since we are using an acoustic-only model, we select those transducer elements that subtend a small angle at the center of the evaluation region with respect to the skull normal to reduce shear wave effects (see Section IIIC). Using these elements, we reconstruct images of the phantoms in the absence of the skull using UBP, and in the presence of the skull using UBP, PSTD, and BEM.

The photographs of the phantoms, the maximum amplitude projections (MAPs) of their respective ground truths, UBP images (using the selected transducers) in the absence of the skull, and UBP, PSTD, and BEM images in the presence of the skull are presented in Fig. 4a. From these images, we observe that the BEM images are the closest to the ground truth, especially in terms of recovering true features and mitigating background artifacts. This is also seen in the line profiles extracted from the phantom images, as shown in Fig. 4b. To quantify the improvement in the sharpness as well as the background in the profiles, we compute their respective standard deviations (treating each profile as a probability density function), and obtain a value of 3.4, 3.7, and 3.2 mm for the UBP, PSTD, and BEM images of phantom A with the skull, respectively, and a value of 3.5, 3.7, and 3.3 mm for the UBP, PSTD, and BEM images of phantom B with the skull, respectively. In contrast, the UBP images of phantoms A and B without the skull have respective standard deviations of 3.1 and 3.3. The T-PAT images reconstructed using BEM also result in the least positional error. We show this in Fig. 4c by overlaying the x-z projections of the envelopes of the reconstructed T-PAT images (green) of a line target on its UBP image in the absence of the skull (magenta). Finally, we quantify the performance of each method using five metrics (averaged over the three phantoms)—correlation coefficient, structural similarity index measure [29] (SSIM), contrast-to-noise ratio (CNR), displacement, and run time—and present them in Fig. 4d. Correlation coefficient and SSIM are computed using the UBP image in the absence of the skull as a reference. Fig. 4d shows that BEM outperforms the other method in terms of all five metrics, except run time, thus demonstrating its superior performance. For clarity, we also present the metrics in Table I.

E. BEM execution time and computational complexity

All simulations were conducted using MATLAB R2023b, deployed on a workstation configured with an Intel Core i9-13900KS processor (3.2 GHz), 4 × 48 GB DDR5 RAM (5200 MHz), and an NVIDIA GeForce RTX 4090 GPU. The operating system used was Windows 11 Pro 23H2. The primary steps in BEM-based transcranial PAT image reconstruction are meshing, operator assembly, incident field computation, solving the linear system, and field evaluation. The first two steps can be performed once for reconstructing a batch of phantom images, provided the geometry and acoustic properties of the skull and the surrounding medium do not change, which gives BEM an additional edge over methods like FDTD and PSTD when reconstructing multiple images. Generating the mesh takes less than a minute at the highest frequency. The operators are assembled using the FFM method, which has a storage complexity of $\mathcal{O}(N)$ and a computational complexity for matrix-vector multiplication of $\mathcal{O}(N \log^2(N))$, where N is proportional to the number of nodes in the mesh. The operator assembly at 0.2 MHz and 0.5 MHz takes around 2 minutes and 20 minutes, respectively. Incident field computation for each

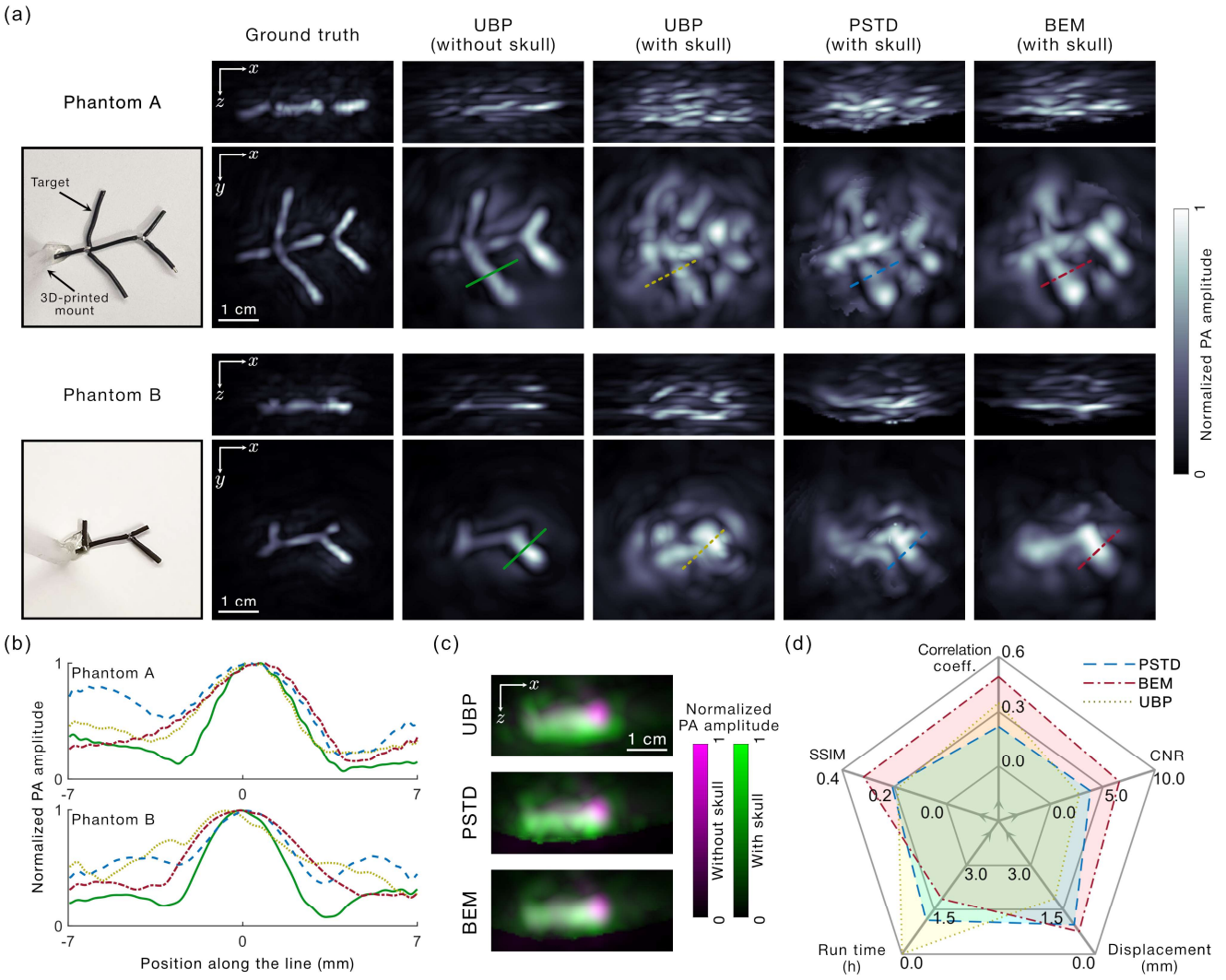

Fig. 4| T-PAT of phantoms through an ex-vivo skull using BEM. (a) Photographs, respective ground truths (UBP images in the absence of the skull reconstructed using all transducer elements), UBP images in the absence of the skull reconstructed using the selected transducer elements, and images through the skull reconstructed using UBP, PSTD, and BEM of the phantoms. (b) Plots of the line profiles extracted from the respective images of the two phantoms in (a). (c) Overlays of the x-z projections of the T-PAT images of a line target obtained using UBP/PSTD/BEM, respectively, shown in green, on the UBP images without the presence of the skull, shown in magenta. This representation shows that the images reconstructed using BEM have the least displacement. (d) Quantitative comparison of UBP, PSTD, and BEM using five metrics (averaged over the three phantoms): correlation coefficient, SSIM, CNR, displacement, and run time. The comparison shows that BEM outperforms PSTD and UBP in all the metrics except run time.

TABLE I
TABULATED QUANTITATIVE METRICS PRESENTED IN FIG. 4D

METRIC	UBP	PSTD	BEM
Correlation coefficient	0.35	0.22	0.49
SSIM	0.19	0.21	0.32
CNR	2.75	3.80	6.57
Displacement (mm)	1.88	0.98	0.75
Run time (mins)	< 1	59	113

phantom at 0.2 MHz and 0.5 MHz takes 1 minute and 6 minutes. Each iteration of GMRES at 0.5 MHz takes half a second, and it takes close to 2.5 minutes to reach a relative error residual of less than 10^{-3}. Evaluating the field for each phantom at 0.2 MHz and 0.5 MHz takes 10 seconds and 40 seconds, respectively. Overall, the reconstruction of one phantom image using BEM takes close to 2 hours (113 minutes). However, reconstruction time per phantom can be lower for a batch of phantoms since the operator assembly, which is the most expensive step, is a one-time cost, provided the geometry and acoustic properties of the skull and the surrounding medium do not change. For instance, the operator assembly and mesh generation steps take 68 minutes out of a total reconstruction time of 113 minutes for a single image. Therefore, by reconstructing a batch of five images, the reconstruction time for a single image can be brought down to 58.5 minutes. In comparison, reconstructing the image of one phantom using PSTD takes around 1 hour.

IV. DISCUSSION

In this paper, we presented a BEM-based acoustic solver for image reconstruction in T-PAT. Our method, which is based on BEM, has several computational advantages over the widely used FDTD/PSTD and FEM-based methods, primarily due to the use of surface meshes in BEM as opposed to volumetric grids and meshes in FDTD/PSTD and FEM, respectively. We demonstrated the computational feasibility of BEM at high

accuracies for practical-sized problems, whereas PSTD is limited by its poor scalability. While we chose to compare our BEM implementation with PSTD due to its popularity in PAT, we refer the readers to [12] for a more comprehensive comparison of different computational techniques for transcranial acoustic propagation. For T-PAT of phantoms through an ex-vivo human skull, we showed that BEM qualitatively and quantitatively outperformed UBP and PSTD, except in terms of run time. Our work demonstrates the natural suitability of BEM to PAT and paves the way for the development of BEM-based image reconstruction approaches in several applications of PAT. It also facilitates clinically relevant applications of T-PAT such as human brain function imaging, stroke and tumor diagnosis and monitoring, and management of traumatic brain injuries [30]–[32].

It is interesting to note that although Fig. 3 shows that BEM is more computationally efficient than PSTD for high accuracies, in the experimental demonstration in Fig. 4, BEM is slower than PSTD. While this may seem counterintuitive, it is due to the higher accuracy that BEM was set up for, which would have been inconveniently expensive to achieve with PSTD. For the reconstructions in Fig. 4, it was stated that the discretization levels for BEM and PSTD were 5 and 6, respectively. From Fig. 3b, we see that this corresponds to an error of 10% for PSTD and 1% for BEM. However, if we use PSTD to obtain the 1% error, we see from Fig. 3b that it would necessitate a discretization level of 16, which would be extremely computationally expensive. Furthermore, this difference keeps increasing as higher levels of accuracy are sought.

A crucial advantage that BEM has compared to other methods, such as PSTD or FDTD, is that the run time of BEM in T-PAT can be significantly optimized by batch reconstructing multiple images. This is because the boundary operator assembly, which is the most expensive step in BEM, can be computed once for multiple images, provided the geometry and the acoustic properties of the skull and the surrounding medium remain the same. This advantage is particularly important in the context of functional imaging, where multiple images are reconstructed across several ON-OFF cycles of functional stimuli [5]. For the same reason, BEM also lends itself naturally to iterative reconstruction schemes [33], where actions of the precomputed boundary operators can be evaluated accurately and efficiently for any number of iterations.

The utility of BEM in PAT is not limited to the problem of T-PAT of the human brain. Detecting hemodynamic changes in response to functional activation in small-animal brains is critical to preclinical studies in neuroscience [4]. At the higher ultrasonic frequencies (> 5 MHz) typically employed in small-animal PAT [2], it is pertinent to correct for the aberrations that small animal skulls cause to optimize image quality. Our approach can be used to model the small-animal skull, particularly in the context of noninvasive imaging. Moving beyond skull aberrations, a common assumption in PAT is that the acoustic properties of soft tissue and water are the same, which justifies the use of image reconstruction methods such as UBP. In several cases, such as small-animal whole-body PAT [2] and human breast PAT [4], the dual speed-of-sound (SoS) UBP method [2], which assigns different SoS values to water and tissue, is commonly used to improve image quality. However, this method does not account for refraction at the water-tissue interface. In such cases, BEM may be used for more accurate modeling of acoustic propagation, thus optimizing the reconstructed image quality in a computationally feasible manner.

Since this is a preliminary study demonstrating the feasibility and suitability of BEM to T-PAT, a few simplifications were made to the experimental setup, which can be improved upon in the future to better mimic the in-vivo situation. In future studies, illumination from outside the skull can be considered with more complex light-absorbing phantoms present both inside and outside the skull. This is to simulate the complex scalp and cortical vasculatures that are present in vivo, where the cortical signals are much weaker than those from the scalp. The strong signals from the scalp and their reflection from the skull present significant challenges to recovering the weak cortical signals in in-vivo T-PAT and will be considered in future studies.

A few improvements can also be made to enhance the performance of BEM for T-PAT. The development of faster and more parallelizable BEM matrix compression and acceleration techniques is one of the most active research topics in BEM [35]–[41]. In our work, we used the fast and free memory method (FFM) [22], which builds on the existing and popular fast multipole method (FMM) and the hierarchical matrix (H-matrix) method [11], to achieve a linear storage complexity compared to the quasi-linear complexity of the aforementioned methods. Notably, we compared our BEM implementation with the one in [42], which uses H-matrices for matrix compression, and found that our implementation outperformed it in terms of accuracy and run time for the benchmark problem in Section III A at frequencies of 0.2 MHz and 0.5 MHz, respectively. Similarly, efforts are also underway to implement methods such as FMM and H-matrices on modern computing architectures such as graphics processing units (GPUs), which will further boost their performance [34], [43]–[45].

The current BEM solver does not account for acoustic attenuation and heterogeneities within the skull. Frequency-dependent acoustic attenuation and dispersion in the skull can be readily incorporated into our method since it is formulated in the frequency domain. The heterogeneity of the skull can also be partially considered by using a three-layer approach that models the skull as three homogeneous layers comprising a trabecular bone layer sandwiched between two cortical bone layers. Certain formulations of BEM exist, such as the dual-reciprocity BEM and the analog equation method, which transform domain integrals into boundary integrals numerically and therefore can deal with inhomogeneities in the medium [10]. However, these methods come at the cost of mathematical, implementation, and computational complexity. Another approach for dealing with inhomogeneities is to use a hybrid FEM-BEM approach [46], where FEM is used to model the inhomogeneous medium (skull) and BEM is used to model the homogeneous (and typically unbounded) exterior domain. However, combining the two techniques increases the computational cost compared to BEM and may require extra care to solve, particularly in cases where interior resonances exist [47]. Nevertheless, the accurate estimation of skull

properties from adjunct images such as X-ray CT remains an open quest [48]. Finally, modeling shear wave effects in the skull is another promising direction that will significantly improve the de-aberrated image quality [49], [50].

APPENDIX A: NUMERICAL PHANTOM RECONSTRUCTION EXPERIMENTS

We conducted numerical phantom reconstruction tests to evaluate the effect of various parameters on BEM-based T-PAT image reconstruction. First, we performed a forward simulation using PSTD with a fine discretization of $\lambda/20$ (on a smaller grid than the one used for the experimental phantom reconstruction in Fig. 4) at the highest considered frequency of 0.5 MHz to ensure high accuracy. Then, we added white Gaussian noise to the signals with a signal-to-noise ratio of 20 dB and reconstructed images of the target using BEM and UBP, respectively. A schematic of the simulation is shown in Fig. 5a. A cross-shaped initial pressure target (2.4 cm × 2.4 cm size) is propagated through a homogeneous hemispherical shell centered at $(0, 0, 2)$ cm with a radius, speed of sound, and density of 4 cm, 3000 m/s, and 1800 kg/m^3, respectively, with water as the background medium. A hemispherical detection surface centered at $(0, 0, 0)$ cm of radius 5.5 cm surrounds the hemispherical shell.

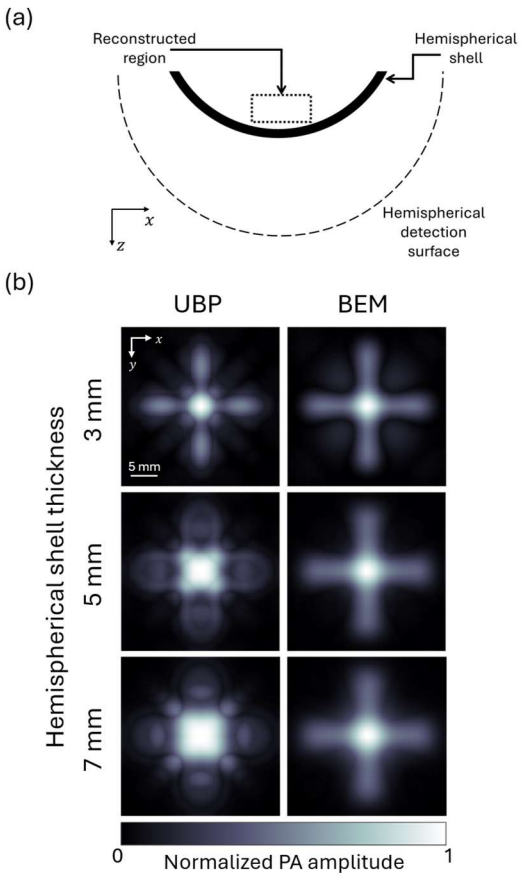

Fig. 5| (a) Schematic of the 3D simulation setup. (b) Images of a simulated cross-target (of size 2.4 cm × 2.4 cm), which were imaged through hemispherical shells of thicknesses ranging from 3 mm to 7 mm, reconstructed using UBP and BEM, respectively.

We test the effect of the shell thickness on the reconstruction. To do this, we perform forward simulations for shell thicknesses of 3 mm, 5 mm, and 7 mm, respectively. The respective reconstructed images using BEM and UBP for different skull thicknesses are shown in Fig. 5b, and it shows that the BEM image reconstruction scheme can correct the aberrations induced by the hemispherical shell for all the considered thicknesses. However, since we did not use an iterative reconstruction scheme, there is a slight degradation in the BEM-reconstructed images with increasing thickness, likely due to the worsening of the propagation operator conditioning. This is linked to the fact that the skull reflects (partially within the critical angle and totally beyond it) the acoustic waves away from the detection surface, which results in either lossy or no detection at different angles (the critical angle at the water-skull interface for the given acoustic properties is 30°). Additionally, we also studied the effect of the speed of sound and density mismatch on the reconstructed images and found that the correlation coefficient of the image reconstructed with a speed of sound mismatch of 10% with the image reconstructed using the true parameters was around 0.88, whereas a 10% density mismatch resulted in a change in the correlation of less than 0.01.

APPENDIX B: EFFECT OF EDGE-MODELING ACCURACY ON BEM

The BEM-reconstructed images shown in Fig. 4 were obtained by extracting the skull shape from an X-ray CT scan of the ex-vivo skull acquired at a resolution of 0.35 mm. To evaluate whether this resolution affects the accuracy at a frequency of 0.5 MHz (~3 mm wavelength in water), we make use of the simulation setup in Appendix A. The hemispherical shell volume is originally at a discretization of 0.15 mm. We reconstruct images of the cross-target using BEM by extracting the hemispherical shell surface from volumes discretized at 0.15 mm, 0.3 mm, 0.6 mm, and 1.2 mm, respectively, and show them in Fig. 6. We also compute the correlation coefficient and

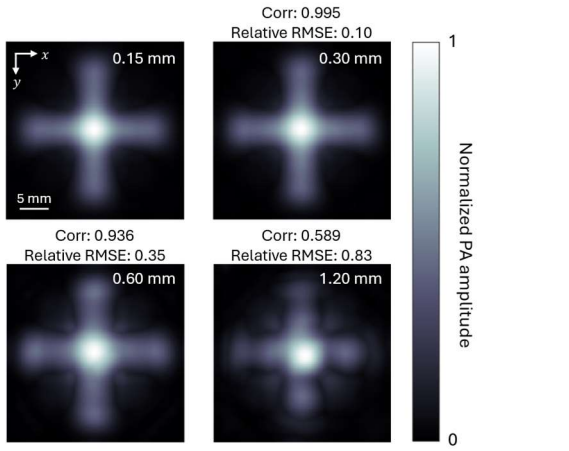

Fig. 6| BEM-reconstructed images of a cross-target through a hemispherical shell obtained by extracting the shell surface at a discretization of 0.15 mm, 0.3 mm, 0.6 mm, and 1.2 mm, respectively. The correlation coefficients and relative RMSEs of the images obtained with a discretization of 0.3 mm and above are computed with respect to the image obtained at 0.15 mm.

relative RMSE for the images acquired at 0.3 mm and above relative to the baseline image acquired at 0.15 mm and present them on top their respective images in Fig. 6. We see from here that the image corresponding to the 0.3 mm discretization (which is the closest to the resolution of the X-ray CT image) is very close to the baseline image, thus corroborating that the resolution of the X-ray CT volume of the ex-vivo skull is sufficient for the frequencies under consideration. However, we also observe a deterioration in the image quality at a discretization of 0.6 mm, which worsens significantly at 1.2 mm. This suggests that it would be necessary to obtain the skull shape at a finer resolution to maintain the accuracy at higher frequencies.

ACKNOWLEDGMENT

L.V.W. has a financial interest in Microphotoacoustics, Inc., CalPACT, LLC, and Union Photoacoustic Technologies, Ltd., which, however, did not support this work.

REFERENCES

[1] L. V. Wang and S. Hu, "Photoacoustic tomography: in vivo imaging from organelles to organs," *Science*, vol. 335, no. 6075, pp. 1458–1462, 2012.

[2] L. Li, L. Zhu, C. Ma, L. Lin, J. Yao, L. Wang, K. Maslov, R. Zhang, W. Chen, and J. Shi, "Single-impulse panoramic photoacoustic computed tomography of small-animal whole-body dynamics at high spatiotemporal resolution," *Nat. Biomed. Eng.*, vol. 1, no. 5, pp. 1–11, 2017.

[3] P. Wray, L. Lin, P. Hu, and L. V. Wang, "Photoacoustic computed tomography of human extremities," *J. Biomed. Opt.*, vol. 24, no. 2, pp. 026003–026003, 2019.

[4] L. Lin, P. Hu, X. Tong, S. Na, R. Cao, X. Yuan, D. C. Garrett, J. Shi, K. Maslov, and L. V. Wang, "High-speed three-dimensional photoacoustic computed tomography for preclinical research and clinical translation," *Nat. Commun.*, vol. 12, no. 1, p. 882, 2021.

[5] S. Na, J. J. Russin, L. Lin, X. Yuan, P. Hu, K. B. Jann, L. Yan, K. Maslov, J. Shi, D. J. Wang, C. Y. Liu, and L. V. Wang, "Massively parallel functional photoacoustic computed tomography of the human brain," *Nat. Biomed. Eng.*, vol. 6, no. 5, pp. 584–592, 2022.

[6] S. Na and L. V. Wang, "Photoacoustic computed tomography for functional human brain imaging," *Biomed. Opt. Express*, vol. 12, no. 7, pp. 4056–4083, 2021.

[7] K. Mitsuhashi, J. Poudel, T. P. Matthews, A. Garcia-Uribe, L. V. Wang, and M. A. Anastasio, "A Forward-Adjoint Operator Pair Based on the Elastic Wave Equation for Use in Transcranial Photoacoustic Computed Tomography," *SIAM J. Imaging Sci.*, vol. 10, no. 4, pp. 2022–2048, Jan. 2017.

[8] Y. Aborahama, K. Sastry, M. Cui, Y. Zhang, Y. Luo, R. Cao, and L. V. Wang, "De-aberration for transcranial photoacoustic computed tomography through an adult human skull," *ArXiv Prepr. ArXiv240405937*, 2024.

[9] Y. Luo, H.-K. Huang, K. Sastry, P. Hu, X. Tong, J. Kuo, Y. Aborahama, S. Na, U. Villa, and M. A. Anastasio, "Full-wave Image Reconstruction in Transcranial Photoacoustic Computed Tomography using a Finite Element Method," *IEEE Trans. Med. Imaging*, 2024.

[10] K. H. Yu, A. H. Kadarman, and H. Djojodihardjo, "Development and implementation of some BEM variants—A critical review," *Eng. Anal. Bound. Elem.*, vol. 34, no. 10, pp. 884–899, 2010.

[11] L. Ying, "Fast Algorithms for Boundary Integral Equations," in *Multiscale Modeling and Simulation in Science*, vol. 66, B. Engquist, P. Lötstedt, and O. Runborg, Eds. Berlin, Heidelberg: Springer Berlin Heidelberg, 2009, pp. 139–193.

[12] J.-F. Aubry, O. Bates, C. Boehm, K. Butts Pauly, D. Christensen, C. Cueto, P. Gélat, L. Guasch, J. Jaros, and Y. Jing, "Benchmark problems for transcranial ultrasound simulation: Intercomparison of compressional wave models," *J. Acoust. Soc. Am.*, vol. 152, no. 2, pp. 1003–1019, 2022.

[13] E. van't Wout, P. Gélat, T. Betcke, and S. Arridge, "A fast boundary element method for the scattering analysis of high-intensity focused ultrasound," *J. Acoust. Soc. Am.*, vol. 138, no. 5, pp. 2726–2737, 2015.

[14] S. L. Jacques, "Optical properties of biological tissues: a review," *Phys. Med. Biol.*, vol. 58, no. 11, p. R37, 2013.

[15] B. A. Auld, in *Acoustic fields and waves in solids*, vol. 2, Рипол Классик, 1973, pp. 1–62.

[16] L. V. Wang and H. Wu, in *Biomedical optics: principles and imaging*, John Wiley & Sons, 2012, pp. 283–322.

[17] T. Betcke, E. Van 'T Wout, and P. Gélat, "Computationally Efficient Boundary Element Methods for High-Frequency Helmholtz Problems in Unbounded Domains," in *Modern Solvers for Helmholtz Problems*, D. Lahaye, J. Tang, and K. Vuik, Eds. Cham: Springer International Publishing, 2017, pp. 215–243.

[18] J.-C. Nédélec, in *Acoustic and Electromagnetic Equations*, New York, NY: Springer New York, 2001, pp. 110–149.

[19] Z. Chen, G. Hofstetter, and H. Mang, "A Galerkin–type BE–formulation for Acoustic Radiation and Scattering of Structures with Arbitrary Shape," in *Computational Acoustics of Noise Propagation in Fluids - Finite and Boundary Element Methods*, S. Marburg and B. Nolte, Eds. Berlin, Heidelberg: Springer Berlin Heidelberg, 2008, pp. 435–458.

[20] M. W. Scroggs, "Efficient computation and applications of the Calderón projector," PhD Thesis, UCL (University College London), 2020.

[21] F. Alouges and M. Aussal, "FEM and BEM simulations with the Gypsilab framework," *SMAI J. Comput. Math.*, vol. 4, pp. 297–318, 2018.

[22] M. Aussal and M. Bakry, "The Fast and Free Memory method for the efficient computation of convolution kernels," *ArXiv Prepr. ArXiv190905600*, 2019.

[23] E. Van 'T Wout, S. R. Haqshenas, P. Gélat, T. Betcke, and N. Saffari, "Benchmarking preconditioned boundary integral formulations for acoustics," *Int. J. Numer. Methods Eng.*, vol. 122, no. 20, pp. 5873–5897, Oct. 2021.

[24] Y. Saad and M. H. Schultz, "GMRES: A Generalized Minimal Residual Algorithm for Solving Nonsymmetric Linear Systems," *SIAM J. Sci. Stat. Comput.*, vol. 7, no. 3, pp. 856–869, Jul. 1986.

[25] O. A. Godin, "Scattering of a spherical wave by a small sphere: An elementary solution," *J. Acoust. Soc. Am.*, vol. 130, no. 4, pp. EL135–EL141, 2011.

[26] B. E. Treeby and B. T. Cox, "k-Wave: MATLAB toolbox for the simulation and reconstruction of photoacoustic wave fields," *J. Biomed. Opt.*, vol. 15, no. 2, pp. 021314–021314, 2010.

[27] A. P. Tran, S. Yan, and Q. Fang, "Improving model-based functional near-infrared spectroscopy analysis using mesh-based anatomical and light-transport models," *Neurophotonics*, vol. 7, no. 1, pp. 015008–015008, 2020.

[28] M. Xu and L. V. Wang, "Universal back-projection algorithm for photoacoustic computed tomography," *Phys. Rev. E*, vol. 71, no. 1, p. 016706, 2005.

[29] Z. Wang, A. C. Bovik, H. R. Sheikh, and E. P. Simoncelli, "Image quality assessment: from error visibility to structural similarity," *IEEE Trans. Image Process.*, vol. 13, no. 4, pp. 600–612, 2004.

[30] S. Yang, D. Xing, Y. Lao, D. Yang, L. Zeng, L. Xiang, and W. R. Chen, "Noninvasive monitoring of traumatic brain injury and post-traumatic rehabilitation with laser-induced photoacoustic imaging," *Appl. Phys. Lett.*, vol. 90, no. 24, 2007.

[31] X. Yang, Y.-H. Chen, F. Xia, and M. Sawan, "Photoacoustic imaging for monitoring of stroke diseases: A review," *Photoacoustics*, vol. 23, p. 100287, 2021.

[32] G. Ku, X. Wang, X. Xie, G. Stoica, and L. V. Wang, "Imaging of tumor angiogenesis in rat brains in vivo by photoacoustic tomography," *Appl. Opt.*, vol. 44, no. 5, pp. 770–775, 2005.

[33] J. Poudel, S. Na, L. V. Wang, and M. A. Anastasio, "Iterative image reconstruction in transcranial photoacoustic tomography based on the elastic wave equation," *Phys. Med. Biol.*, vol. 65, no. 5, p. 055009, 2020.

[34] T. Takahashi and T. Hamada, "GPU-accelerated boundary element method for Helmholtz' equation in three dimensions," *Int. J. Numer. Methods Eng.*, vol. 80, no. 10, pp. 1295–1321, Dec. 2009.

[35] C. Bauinger and O. P. Bruno, "'Interpolated factored green function' method for accelerated solution of scattering problems," *J. Comput. Phys.*, vol. 430, p. 110095, 2021.

[36] C. Bauinger and O. P. Bruno, "Massively parallelized interpolated factored Green function method," *J. Comput. Phys.*, vol. 475, p. 111837, 2023.

[37] M. Bebendorf and S. Rjasanow, "Adaptive Low-Rank Approximation of Collocation Matrices," *Computing*, vol. 70, no. 1, pp. 1–24, Feb. 2003.

[38] S. Börm and J. M. Melenk, "Approximation of the high-frequency Helmholtz kernel by nested directional interpolation: error analysis," *Numer. Math.*, vol. 137, pp. 1–34, 2017.

[39] S. Börm, "Directional -matrix compression for high-frequency problems," *Numer. Linear Algebra Appl.*, vol. 24, no. 6, p. e2112, Dec. 2017.

[40] B. Engquist and L. Ying, "Fast Directional Multilevel Algorithms for Oscillatory Kernels," *SIAM J. Sci. Comput.*, vol. 29, no. 4, pp. 1710–1737, Jan. 2007.

[41] M. Messner, M. Schanz, and E. Darve, "Fast directional multilevel summation for oscillatory kernels based on Chebyshev interpolation," *J. Comput. Phys.*, vol. 231, no. 4, pp. 1175–1196, 2012.

[42] E. van't Wout, R. Haqshenas, and P. Gélat, "Simulating Focused Ultrasound with the Boundary Element Method," in *2024 IEEE UFFC Latin America Ultrasonics Symposium (LAUS)*, 2024, pp. 1–4.

[43] N. A. Gumerov and R. Duraiswami, "Fast multipole methods on graphics processors," *J. Comput. Phys.*, vol. 227, no. 18, pp. 8290–8313, 2008.

[44] K. Vater, T. Betcke, and B. Dilba, "Simple and efficient GPU parallelization of existing H-Matrix accelerated BEM code." arXiv, 06-Nov-2017.

[45] P. Zaspel, "Algorithmic patterns for H-matrices on many-core processors," *J. Sci. Comput.*, vol. 78, no. 2, pp. 1174–1206, 2019.

[46] R. Hiptmair and P. Meury, "Stabilized FEM-BEM Coupling for Helmholtz Transmission Problems," *SIAM J. Numer. Anal.*, vol. 44, no. 5, pp. 2107–2130, Jan. 2006.

[47] E. van't Wout, "Stable and efficient FEM-BEM coupling with OSRC regularisation for acoustic wave transmission," *J. Comput. Phys.*, vol. 450, p. 110867, 2022.

[48] T. D. Webb, S. A. Leung, J. Rosenberg, P. Ghanouni, J. J. Dahl, N. J. Pelc, and K. B. Pauly, "Measurements of the relationship between CT Hounsfield units and acoustic velocity and how it changes with photon energy and reconstruction method," *IEEE Trans. Ultrason. Ferroelectr. Freq. Control*, vol. 65, no. 7, pp. 1111–1124, 2018.

[49] A. F. Seybert, T. W. Wu, and X. F. Wu, "Radiation and scattering of acoustic waves from elastic solids and shells using the boundary element method," *J. Acoust. Soc. Am.*, vol. 84, no. 5, pp. 1906–1912, 1988.

[50] P. P. Goswami, T. J. Rudolphi, F. J. Rizzo, and D. J. Shippy, "A boundary element model for acoustic-elastic interaction with applications in ultrasonic NDE," *J. Nondestruct. Eval.*, vol. 9, pp. 101–112, 1990.